Modelling surface roughening during plastic deformation of metal crystals under contact shear loading

Irani, Nilgoon; Nicola, Lucia

DOI
10.1016/j.mechmat.2019.02.007

Publication date
2019

Document Version
Accepted author manuscript

Published in
Mechanics of Materials

Modelling surface roughening during plastic deformation of metal crystals under contact shear loading

Nilgoon Irani[a,*], Lucia Nicola[a,b]

[a] *Department of Materials Science and Engineering, Delft University of Technology, 2628 CD Delft, The Netherlands*
[b] *Department of Industrial Engineering, University of Padova, 35131 Padua, Italy*

Abstract

During plastic deformation, metal surfaces roughen and this has a deleterious impact on their tribological performance. It is therefore desirable to be able to predict and control the amount of roughening caused by subsurface plasticity. As a first step, we focus on modelling plastic deformation during contact shearing of an FCC metallic single crystal, employing a finite strain Discrete Dislocation Plasticity (DDP) formulation. This formulation allows us to capture the finite lattice rotations induced in the material by shearing and the corresponding local rotation of the crystallographic slip planes. The simulations predict a pronounced material pile-up in front of the contact and a sink-in at its rear, which are strongly crystal-orientation dependent. By comparing finite and small strain DDP, we can assess the effect of slip plane rotation on surface roughening and on metal plasticity in general. Results of the simulations are also compared with crystal plasticity, which is also capable of predicting a pile-up and sink-in, but not the crystal-orientation dependency of roughening.

Keywords: Contact shearing, Surface roughening, Dislocations, Finite strains, Size effects

1. Introduction

Tribological metal contacts are subjected to surface roughening induced by subsurface plastic strains and strain gradients (Karthikeyan et al., 2005; Rigney and Karthikeyan, 2010). Roughening can promote wear and degrade the performance of the rubbing materials, by that affecting their life time (Wilson et al., 1981; Romanova et al., 2013). It is therefore important to be able to predict and possibly control plastic roughening. This is even more relevant in micro-machines, where surface effects are dominant. This work aims at shading light on the effect of dislocation plasticity and crystal orientation on surface roughening.

Recent experiments by Brinckmann and Dehm (2015) showed that scratching by micro-sized tools results in plastic ploughing and surface slip markings. The markings are the signature of dislocations gliding out of the surface. Moreover, they found that local crystal orientation has a significant influence on the development and spread of plasticity and surface deformation.

Several numerical studies have been performed to examine micro-scale plasticity and surface deformation. For example, using two-dimensional discrete dislocation plasticity (DDP) shearing of crystals has been performed by Deshpande et al. (2004), Song et al. (2016), Sun et al. (2016) and Ng Wei Siang and Nicola (2017). These works have shown that during plastic deformation pronounced crystallographic steps appear on the surface of the material, when dislocations glide out of a free surface. More recently, Gagel et al. (2018), performed three-dimensional DDP simulations of an asperity sliding over a metal crystal. Based on their calculations, they concluded that as an asperity moves on the metal surface, transport of dislocations may largely influence the plastic deformation and the stemming surface topology. All these numerical analyses were performed under the assumption of small strains and hence, effects of finite lattice rotations and shape

*Corresponding author *E-mail address:* n.irani@tudelft.nl

changes due to deformation and dislocation slip were neglected. However, both these effects are expected to play a non-negligible role in the plastic response of the material and its surface roughening (Irani et al., 2017). In this paper, we present a finite strain analysis of the shearing of a metallic FCC single crystal by a rigid solid. The primary aim of this study is to identify how and to what extend finite deformations influence the plastic response and the resultant surface profile in metals. To tackle this question we will use both the small strain DDP method of Van der Giessen and Needleman (1995) and the finite strain DDP formulation of Irani et al. (2015). Crystal plasticity (CP) results are also presented to asses its limitations when modelling the deformation of a single crystal. Note that the finite strain formulation is used only for rather small deformations, because the method does not yet include remeshing and can therefore not be applied for very large strains.

The outline of the paper is as follows: First, the employed DDP formulations, as well as the employed CP method, are presented. Second, the small and finite strain DDP calculations of the plastic response are discussed for a crystal sheared by rigid solids of different size. The effects of crystal orientation and nucleation source density are investigated. Finally, the surface roughening profiles for all these cases as obtained by small and finite strain DDP as well as CP simulations are presented and discussed. It is worth noting that in the current study the finite strain effects considered are lattice rotations and shape changes caused by dislocation slip. Any impact of heat and thermal expansion is ignored. Cases involving abrasion, i.e. fracture and removal of the base material are also excluded from this work.

2. Formulation of the problem

The 2D model of a single crystal sheared by a rigid solid of width W is shown in Fig. 1. This is an idealized representation of the contact between a metal surface and a tool or a hard contaminant particle. Plane

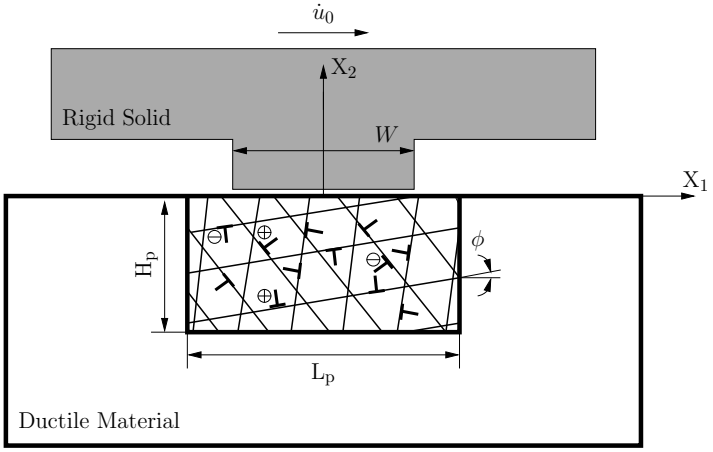

Figure 1: Schematic representation of a single crystal sheared by a rigid solid. The coordinate system and critical dimensions are indicated, as well as some slip planes and dislocations in the plastic zone. The convention employed for the sign of the edge dislocations is also shown.

strain conditions are assumed with deformations restricted to the X_1-X_2 plane. The surface of the crystal is considered to be flat and smooth, and to be in perfect adhesive contact with the rigid solid which shears the crystal by moving at constant speed in the tangential direction. Thus, the boundary conditions at the contact are given by

$$\dot{u}_1 = \dot{u}_0,\ \dot{u}_2 = 0. \tag{1a}$$

All other surfaces have traction-free boundary conditions except the bottom surface, where

$$\dot{u}_1 = \dot{u}_2 = 0. \tag{1b}$$

In this work, results are presented in terms of the contact shear stress

$$\tau = \frac{1}{W} \int_{S_C} T_1 \, \mathrm{d}s. \tag{2}$$

The integration above is performed along the contact area $S_C = \{-W/2 \leq X_1 \leq W/2 \text{ and } X_2 = 0\}$ and T_1 are the tractions in the X_1 direction. To limit simulation time, plasticity is assumed to be confined to a rectangular window of $\mathrm{L_p} \times \mathrm{H_p}$ inside of which dislocations are treated discretely. The window is taken to be sufficiently large so that the dislocations do not reach its boundary during the simulations. The dislocations that impinge on the contact are not allowed to penetrate the rigid solid. To establish this condition, impenetrable obstacles are placed at the end of the slip planes just below the contact region.

2.1. Small strain discrete dislocation plasticity

At time t, the body under study contains N discrete edge dislocations represented as line singularities in an elastic domain (Van der Giessen and Needleman, 1995). In the small strain DDP, the aim is to solve the equilibrium equation

$$\sigma_{ij,j} = 0, \tag{3}$$

along with the corresponding boundary conditions. Here, $(\,)_{,i} \equiv \partial(\,)/\partial X_i$ are the spatial gradients in the undeformed configuration. Boundary conditions are specified as

$$T_i = T_i^0 \;\text{ on } S_T, \tag{4}$$

$$u_i = u_i^0 \;\text{ on } S_U, \tag{5}$$

where T_i and u_i are tractions and displacements, respectively. In this method, the fields are calculated using superposition of: (i) singular ($\tilde{}$) fields of the N dislocations which are computed analytically and (ii) the image ($\hat{}$) fields which ensure the boundary conditions are satisfied. Thus, displacements, strains and stresses are expressed as

$$u_i = \hat{u}_i + \tilde{u}_i, \qquad \varepsilon_{ij} = \hat{\varepsilon}_{ij} + \tilde{\varepsilon}_{ij}, \qquad \sigma_{ij} = \hat{\sigma}_{ij} + \tilde{\sigma}_{ij}, \tag{6}$$

while the analytical fields of the discrete dislocations are:

$$\tilde{u}_i = \sum_{I=1}^{N} \tilde{u}_i^{(I)}, \qquad \tilde{\varepsilon}_{ij} = \sum_{I=1}^{N} \tilde{\varepsilon}_{ij}^{(I)}, \qquad \tilde{\sigma}_{ij} = \sum_{I=1}^{N} \tilde{\sigma}_{ij}^{(I)}. \tag{7}$$

Unlike the dislocation fields, the ($\hat{}$) fields are smooth and they are obtained by using the conventional finite element method, while solving

$$\int_{\Omega} \hat{\sigma}_{ij} \, \hat{\eta}_{i,j} \, \mathrm{d}\Omega = \int_{S_T} (T_i^0 - \tilde{T}_i) \, \hat{\eta}_i \, \mathrm{d}S, \tag{8}$$

where $\hat{\eta}_i$ are arbitrary continuous displacement fields.

2.1.1. Constitutive rules

The Peach-Koehler force $f^{(I)}$ on dislocation I is calculated as

$$f^{(I)} = \left(\hat{\sigma}_{ij} + \sum_{J \neq I} \tilde{\sigma}_{ij}^{(J)} \right) b_j^{(I)} m_i^{(\alpha)}. \tag{9}$$

Here, $\tilde{\sigma}_{ij}^{(J)}$ is the stress field of dislocation J at the position of dislocation I. The Burgers vector of dislocation I is shown by $b_j^{(I)}$ and the unit vector normal to slip plane α is indicated by $m^{(\alpha)}$. The glide velocity $v^{(I)}$ of dislocation I has a linear relation with the Peach-Koehler force $f^{(I)}$:

$$v^{(I)} = \frac{1}{B} f^{(I)}, \tag{10}$$

where B is the drag coefficient. New dislocation pairs are generated by randomly distributed Frank-Read sources. Nucleation occurs when the Peach-Koehler force $f^{(I)}$ on source I exceeds $\tau_{\text{nuc}}b$ for a time period t_{nuc}. Furthermore, two opposite signed dislocations on a slip plane annihilate each other if they are within the distance L_{e}. An Obstacle pins a dislocation, as it tries to glide through this obstacle. When the Peach-Koehler force on the obstacle becomes larger than $\tau_{\text{obs}}b$, the dislocation is released from the Obstacle.

2.2. Finite strain discrete dislocation plasticity

The finite strain DDP framework, in contrast to the small strain calculations, accounts for: (i) lattice rotations and (ii) shape changes due to slip. The aim of finite strain DDP is to solve the equilibrium equation

$$\sigma_{ij;j} = 0, \tag{11}$$

along with the boundary conditions for this equation. Here, $(\ )_{;i} \equiv \partial(\ )/\partial x_i$ are the spatial gradients in the deformed configuration. In this method, for each time-step the total displacement *rate* is decomposed into the analytically known ($\tilde{}$) dislocation fields and the ($\hat{}$) fields which ensure the boundary conditions are satisfied:

$$\dot{u}_i(X_j, t) = \dot{\hat{u}}_i(X_j, t) + \dot{\tilde{u}}_i(X_j, t), \tag{12}$$

where X_j is the position of a material point in the undeformed configuration. Hence, the material and lattice velocity gradients, $\dot{u}^{\text{m}}_{i,j}$ and $\dot{u}^{\text{e}}_{i,j}$ are

$$\dot{u}^{\text{m}}_{i,j} = \dot{\hat{u}}_{i,j} + \dot{\tilde{u}}^{\text{d}}_{i,j}, \tag{13}$$

$$\dot{u}^{\text{e}}_{i,j} = \dot{\hat{u}}_{i,j} + \dot{\tilde{u}}_{i,j}, \tag{14}$$

respectively. The gradient $\dot{\tilde{u}}^{\text{d}}_{i,j}$ is calculated by the numerical differentiation of the velocity field $\dot{\tilde{u}}_i$ with respect to X_j using the finite element shape functions in the undeformed configuration. Besides, $\dot{\tilde{u}}_{i,j}$ is obtained by analytical differentiation of $\dot{\tilde{u}}_i$ with respect to X_j. Moreover, the Cauchy stress field σ_{ij} is given by

$$\sigma_{ij} = \hat{\sigma}_{ij} + \tilde{\sigma}_{ij}. \tag{15}$$

Recall that $\tilde{\sigma}_{ij}$ is an equilibrium field. Hence, the weak form of the equilibrium equation (11) simplifies to

$$\int_{\Omega^*} \hat{\sigma}_{ij}\, \hat{\eta}_{i;j}\, \mathrm{d}\Omega = \int_{S_T^*} (T_i^* - \tilde{T}_i^*)\, \hat{\eta}_i\, \mathrm{d}S, \tag{16}$$

where Ω^* is the domain in its deformed configuration and T_i^* and $\tilde{T}_i$ are the tractions specified on the boundary S_T^* in the deformed configuration. Displacement boundary conditions are also specified on S_U^*. The deformation gradient is given by $F_{ij} = \delta_{ij} + u^{\text{m}}_{i,j}$, where δ_{ij} is the Kronecker delta. Hence, the 2nd Piola-Kirchhoff stress S_{ij} is obtained as

$$S_{ij} = F^{-1}_{im}\, \sigma_{mn}\, F^{-1}_{jn}\, J, \tag{17}$$

where $J \equiv \det(F_{ij})$. Relation (15) implies that

$$\hat{S}_{ij} = F^{-1}_{im}\, \hat{\sigma}_{mn}\, F^{-1}_{jn}\, J, \tag{18a}$$

and

$$\tilde{S}_{ij} = F^{-1}_{im}\,\tilde{\sigma}_{mn}\,F^{-1}_{jn}\,J, \tag{18b}$$

such that $S_{ij} = \hat{S}_{ij} + \tilde{S}_{ij}$. Using Eq. (18a) along with Eq. (13), the weak form of the equilibrium equation (16) in the undeformed configuration is written as

$$\int_{\Omega} \left(\hat{S}_{ij}\,\hat{\eta}_{i,j} + \hat{S}_{ij}\,\hat{u}_{k,i}\,\hat{\eta}_{k,j} \right) \mathrm{d}\Omega = \int_{S^*_T} (T^*_i - \tilde{T}^*_i)\,\hat{\eta}_i\,\mathrm{d}S - \int_{\Omega} \left(\hat{S}_{ij}\,\tilde{u}^{\mathrm{d}}_{k,i}\,\hat{\eta}_{k,j} \right) \mathrm{d}\Omega, \tag{19}$$

where Ω is the domain in its undeformed configuration. Finally, the constitutive relations for S_{ij} and $\hat{S}_{ij}$ are obtained analogous to conventional crystal plasticity (Irani et al., 2015, 2017).

The equation (19) along with boundary conditions can be solved by a conventional finite element method. However, dissimilar to the small strain formulation, the $\hat{(\ )}$ field problem is nonlinear and therefore, it should be solved iteratively (Irani et al., 2015, 2017). Here, traction free and displacement boundary conditions are prescribed on the same material points throughout the simulation.

2.2.1. Constitutive rules

In the finite strain model, unlike the small strain DDP, the dislocations do not glide on a straight slip plane. This is because due to finite deformations and lattice rotations, they move may away from a straight path. The local lattice rotation is obtained as

$$\varphi = \sin^{-1}(R_{21}). \tag{20}$$

Here, the rotation tensor $R_{ij} = F^e_{ik}\,U^{-1}_{kj}$, where $U_{ij} = (F^e_{ki}\,F^e_{kj})^{1/2}$. Thus, the slip plane oriented at $\phi^{(\alpha)}$ in the undeformed configuration has locally rotated by φ in the deformed configuration. The Peach-Koehler force $f^{(I)}$ on dislocation I is

$$f^{(I)} = \left(\hat{\sigma}_{ij} + \sum_{J \neq I} \tilde{\sigma}^{(J)}_{ij} \right) b^{*(I)}_j m^{*(\alpha)}_i, \tag{21}$$

where $\tilde{\sigma}^{(J)}_{ij}$ is the stress field of dislocation J at the position of dislocation I. Moreover, $b^{*(I)}_j$ is the Burgers vector of dislocation I and $m^{*(\alpha)}$ is the unit vector normal to slip plane α, where both are defined in the deformed configuration. Similar to small strain DDP, new dislocation pairs are generated by Frank-Read sources. Differently from small strain DDP, the discrete point sources belong to a slip system rather than a slip plane and the Burgers vectors of the nucleated dislocation dipole are aligned with $s^{*(\alpha)}_i$, i.e. the unit vector in the direction of slip system α in the deformed configuration. Opposite signed dislocations on slip system α annihilate when they are closer than L_{e}. In the small strain formulation, opposite signed dislocations may annihilate solely if they are on a given slip plane. However, in the finite strain case opposite signed dislocations annihilate if they are on a given *slip system*. Finally, dislocations which glide on the slip system of an obstacle and are closer than L_{e} from it, get pinned to that obstacle.

2.3. Crystal plasticity

In the following, the surface roughening profiles are also obtained by means of the size-independent visco-plastic continuum crystal plasticity formulation of Peirce et al. (1983). The total strain rate is computed as the sum of an elastic and a viscoplastic part:

$$\dot{\epsilon}_{ij} = \dot{\epsilon}^{\mathrm{e}}_{ij} + \dot{\epsilon}^{\mathrm{p}}_{ij}. \tag{22}$$

The elastic part is given by

$$\dot{\sigma}_{ij} = L_{ijkl}\,\dot{\epsilon}^{\mathrm{e}}_{kl}, \tag{23}$$

where L_{ijkl} is the elastic moduli tensor. The plastic part of the strain rate is written as

$$\dot{\epsilon}^{\mathrm{p}}_{ij} = \sum_{\alpha} \dot{\gamma}^{\alpha}\,\mu^{\alpha}_{ij}, \qquad \mu^{\alpha}_{ij} = \frac{1}{2}(s^{\alpha}_i m^{\alpha}_j + s^{\alpha}_j m^{\alpha}_i), \tag{24}$$

where m_i^α and s_i^α are unit vectors normal to and in the direction of slip system α. Besides, $\dot{\gamma}_\alpha$ is the intrinsic slip rate and its value is given by the following power law relation:

$$\dot{\gamma}_\alpha = \dot{\gamma}_0 \frac{\tau^\alpha}{g^\alpha} \left| \frac{\tau^\alpha}{g^\alpha} \right|^{(1/m)-1}, \tag{25}$$

where $\tau^\alpha = m_i^\alpha \, \sigma_{ij} \, s_j^\alpha$ is the resolved shear stress on slip system α and $\dot{\gamma}_0$ is a reference slip rate. Moreover, m is the strain rate sensitivity exponent and g^α is the hardness of slip system α with an initial value τ_0 for all α. Furthermore, g^α evolves according to

$$\dot{g}^\alpha = h_0 \sum_\alpha |\dot{\gamma}^\alpha|. \tag{26}$$

2.4. Choice of properties

The crystal has a Young's modulus $E = 70$ GPa and a Poisson's ratio $\nu = 0.33$, representative values for aluminium. Simulations are reported for a reference crystallographic configuration representing a FCC metal crystal with three slip systems, where the slip planes are oriented in the original configuration at $\phi_1 = 15\,^\circ$, $\phi_2 = 75\,^\circ$ and $\phi_3 = 135\,^\circ$ with respect to the X_1-axis. The impact of crystal orientation is analysed by repeating the simulations for a crystal rotated by $30\,^\circ$. Three contact sizes $W = 1.0$ μm, 2.0 μm and 4.0 μm are considered. The size of the crystal is 1000 μm $\times$50 μm which is large enough to have a negligible effect on the outcome of the simulations.

In the finite and small strain DDP simulations, the body is initially dislocation-free. Dislocations are nucleated from Frank-Read sources which are randomly distributed on the slip planes with a density $\rho_{\text{src}} = 50$ μm^{-2}. The nucleation sources have a Gaussian strength distribution. The mean source strength is $\bar{\tau}_{\text{nuc}} = 50$ MPa. Moreover, the nucleation time $t_{\text{nuc}} = 10$ ns. The density of obstacles is $\rho_{\text{obs}} = 25$ μm^{-2} and the obstacle strength is $\tau_{\text{obs}} = 150$ MPa. The drag coefficient for glide is $B = 10^{-4}$ Pa s (Kubin et al., 1992) and the critical distance for annihilation is $L_{\text{e}} = 6b$, where $b = 2.5 \times 10^{-4}$ μm is the magnitude of the Burgers vector. Besides, in all calculations a time step of $\Delta t = 0.5$ ns is employed. The DDP simulations are performed for five realisations of nucleation source and obstacle distributions. In the following, the presented results are obtained by averaging over these five realisations.

The crystal plasticity simulation parameters are chosen to fit the small strain DDP simulations for large contacts, i.e. for sizes where plastic shear response is size independent. Accordingly, in the CP simulations the default values for the strength of the slip systems are chosen as $\tau_0 = 50$ MPa and $h_0 = 500$ MPa. The initial slip rate is $\dot{\gamma} = 0.002\,\text{s}^{-1}$ and the rate sensitivity exponent is $m = 1/200$. The finite element mesh size in CP and DDP simulations is identical.

3. Size dependent shearing response

Computed curves of contact shear stress τ versus applied displacement u_1 are shown in Fig. 2(a) for three different contact sizes, $W = 1.0$ μm, 2.0 μm and 4.0 μm. Here, finite strain DDP simulations are contrasted with their small strain counterparts while the same realisations of obstacle and nucleation source distributions are used for both methods. This figure shows that both the DDP simulations result in an elastic response followed by plasticity for all crystals considered. The curves calculated by small and finite strain DDP deviate from each other during plastic deformation. The difference is very pronounced for contact size $W = 1.0$ μm and negligible for $W = 4.0$ μm. The onset of yield is minorly affected, while the hardening slope depends on whether finite deformations are considered or not. We shall emphasise that the difference between the results of small and finite strain DDP are mainly due to finite strain plasticity effects and not due to finite strain elastic effects (see Appendix A).

We now proceed to investigate the reasons behind the observed differences starting from the dislocation densities, ρ_{disl}, presented in Fig. 2(b) as a function of lateral displacement u_1. Here, for all widths W, the dislocation density has been calculated as the ratio of the total number of dislocations to the area of the

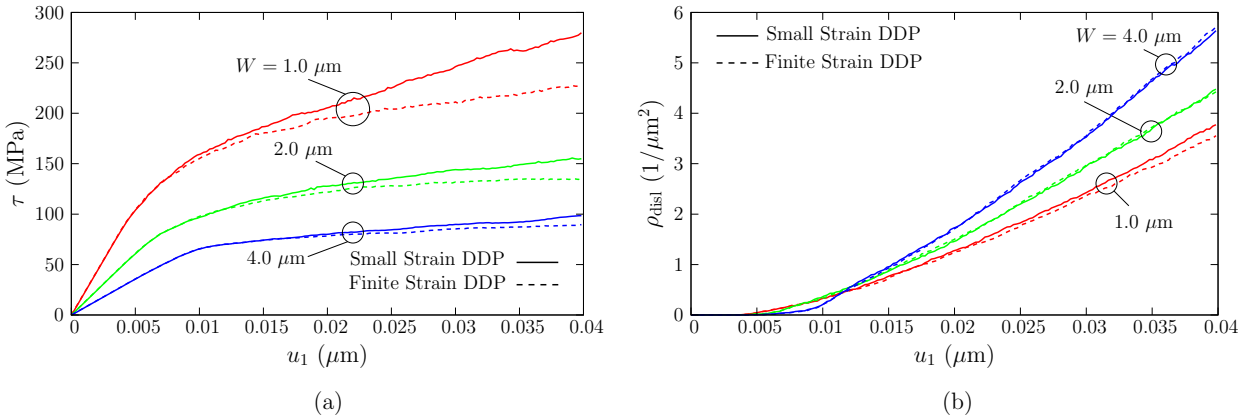

Figure 2: Finite and small strain DDP results of (a) contact shear stress τ and (b) dislocation density ρ_{disl} vs. lateral displacement u_1. Results are shown for three selected widths W of the shearing solid.

process zone, i.e. $\text{L}_\text{p} \times \text{H}_\text{p}$. Here, the dislocation density ρ_{disl} is only employed to compare the finite and small strain predictions. Hence, the assumption of a constant plastic area for all contact sizes is appropriate. Fig. 2(b) demonstrates that the difference between the obtained dislocation densities ρ_{disl} are too small for all widths W to justify the different plastic responses observed in Fig. 2(a). Therefore, we will proceed to examine the estimated plastic slip.

Here, following the work of Balint et al. (2006), plastic slip is calculated by using the values of total displacements u_i at the finite element nodes and evaluating their gradients by numerical differentiation based on the undeformed configuration. One may observe that the definition of slip in this way is mesh dependent. However, as we employ the exact same mesh in both the small and finite strain simulations, the mesh dependency of this definition does not result in any discrepancy when comparing the results. Here, as the calculation of plastic slip is based on the total displacement u_i values, we have included the slip contributions of all the dislocations inside the crystal along the ones that have exited from free surfaces. The slip $\gamma^{(\alpha)}$ is defined by

$$\gamma^{(\alpha)} = s_i^{(\alpha)}(u_{i,j} + u_{j,i})\, m_j^{(\alpha)}. \tag{27}$$

The quantity $\gamma^{(\alpha)}$ is not the actual slip on slip system α as it includes contributions from dislocations on all slip systems. Nevertheless, the slip pattern can conveniently be shown using this parameter. Subsequently, the total slip over the three slip systems is calculated as $\Gamma = \sum_{\alpha=1}^{3} |\gamma^{(\alpha)}|$. Contours of the total slip Γ are shown in Figs. 3(a) and (b) for finite and small strain DDP simulations, respectively. Both figures are obtained for the same realisation and a contact size of $W = 1.0$ μm at $u_1 = 0.04$ μm. This figure demonstrates that during plastic shearing, the imposed deformations are accompanied by the formation of slip bands below and around the contact region. Moreover, a comparison between the slip bands in Figs. 3(a) and (b) shows that while the number of formed slip bands are visually the same, on average, the finite strain calculations correspond to a larger total slip Γ, responsible for the softer shear response obtained with the finite strain calculations.

Figure 3(c) provides a comparison between the dislocation pile-ups obtained by finite and small strain DDP simulations. As it can be observed, the dislocations pile-ups in the finite strain calculations are shorter and less dense when compared to their small strain counterparts. Moreover, the dislocation pile-ups in the finite strain case are not aligned as in these calculations the effect of lattice rotations and finite deformations are included. Consequently, in the finite strain case the dislocations glide more easily and plastic hardening is less. Nevertheless, plastic slip increases significantly with contact area, to such an extent that in large contacts the material displays a perfect plastic response in both the finite and small strain calculations (see Fig. 2(a)).

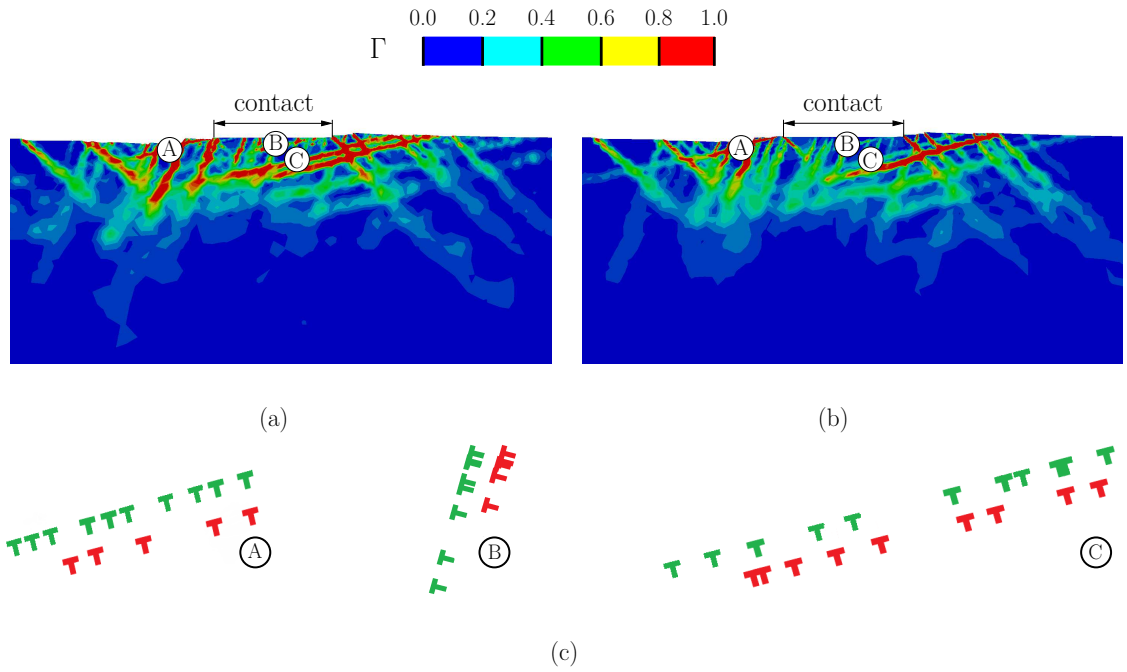

Figure 3: (a) Finite and (b) small strain DDP predictions of total slip Γ at $u_1 = 0.04$ μm for contact size $W = 1.0$ μm. The results are plotted on the deformed configuration where the deformation is magnified by the factor 5. (c) Selection of three dislocation pile-ups obtained by finite (in red) and small (in green) strain DDP simulations.

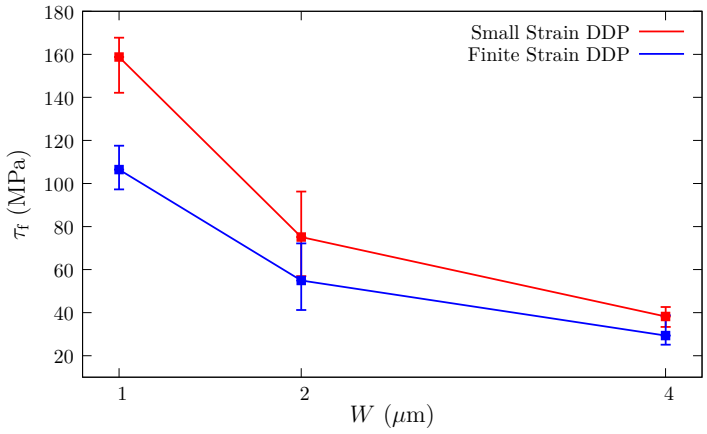

Figure 4: Finite and small strain DDP results of shear flow strength τ_f for various contact sizes W. The error bars indicate the scatter in τ_f values due to different realisations of the source and obstacle distributions.

To summarise, we define the shear flow strength as

$$\tau_{\mathrm{f}} = \tau(u_1 = 0.04\ \mu\mathrm{m}) - \ \tau_{\mathrm{Y}}, \tag{28}$$

where τ_{Y} is the magnitude of shear stress at the point of yielding. The variation of τ_{f} with contact size W is plotted in Fig. 4 for both the small and finite strain calculations.

In this paper, we only discuss the observations made for contact shearing. For the sake of completeness, a short description of the results obtained for indentation by a flat punch are also included in Appendix B.

3.1. Effect of crystal orientation

Here, the crystal under study is obtained by rotating the reference slip orientations by 30° in the counter clockwise direction and is identified by $\phi_1 = 45°$, $\phi_2 = 105°$ and $\phi_3 = 135°$. The current crystal is equivalent to mirroring the reference crystal with respect to the $\mathrm{X}_2-\mathrm{X}_3$ plane and hence, the simulations of this section can also be interpreted as shearing the reference crystal in the opposite direction.

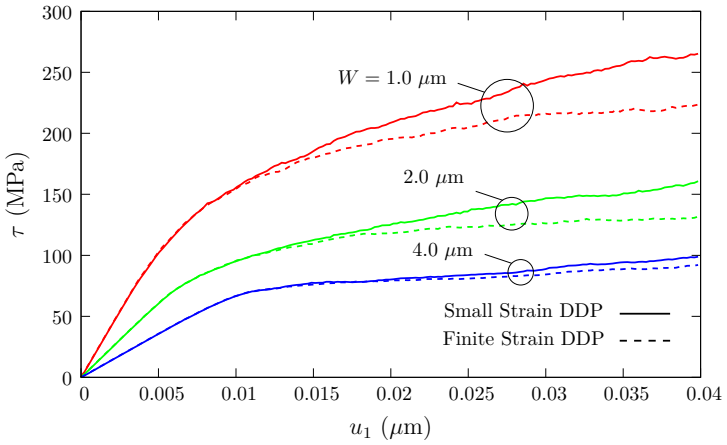

Figure 5: Finite and small strain DDP results of contact shear stress τ vs. lateral displacement u_1. Results are shown for three selected widths W of the shearing solid.

The evolution of contact shear stresses τ with lateral displacement u_1 is shown in Fig. 5 for three selected widths W of the rigid body. The observations obtained from this figure are very similar to the results shown in Fig. 2(a) as both τ and the difference between finite and small strain results decrease with contact size.

3.2. Effect of nucleation source and obstacle density

In this section, we examine the role of source and obstacle densities by analysing crystals with two new sets of parameters: (i) $\rho_{\mathrm{nuc}} = 50\,\mu\mathrm{m}^{-2}$ and $\rho_{\mathrm{obs}} = 50\,\mu\mathrm{m}^{-2}$; (ii) $\rho_{\mathrm{nuc}} = 125\,\mu\mathrm{m}^{-2}$ and $\rho_{\mathrm{obs}} = 25\,\mu\mathrm{m}^{-2}$. The width of the rigid solid is chosen to be $W = 1.0\ \mu$m, the case where the largest difference between small and finite strain DDP calculations was observed (see Fig. 2(a)). The finite and small strain DDP results of the contact shear stress τ for these two cases are shown in Fig. 6. Results for the reference crystal of Section 3 with $\rho_{\mathrm{nuc}} = 50\,\mu\mathrm{m}^{-2}$ and $\rho_{\mathrm{obs}} = 25\,\mu\mathrm{m}^{-2}$ are also repeated here for the purpose of comparison.

Figure 6 demonstrates that even doubling the obstacle density has a negligible impact on both the small and finite strain DDP results. Besides, in both the DDP simulations a higher ρ_{nuc} results in a decrease in yield stress and plastic hardening rate as plastic slip increases with ρ_{nuc}. Consequently, similar to employing a large contact size, increasing the dislocation source density also reduces the difference between the shear stress τ of finite and small strain DDP methods.

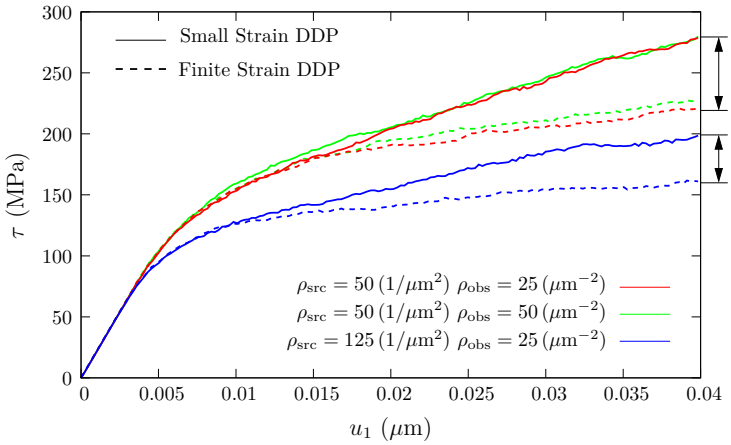

Figure 6: Finite and small strain DDP results of the effect of dislocation source and obstacle density on contact shear stress τ for the rigid body width $W = 1.0$ μm.

4. Surface roughening

During plastic shearing of crystals, surface roughening takes place with material piling-up in front of the contact and sinking in behind it. A schematic representation of this phenomenon is shown in Fig. 7. This figure also represents the definition of the two roughening parameters employed in this work: (i) The material pile-up height R_{H}, which is defined as the distance between the highest point of the profile and the original surface and (ii) The distance between the deepest valley of the profile and the original surface which is called the material sink-in depth R_{D}. In industrial applications, R_{H} is used to check the size of protrusions as it affects both static and sliding contacts. In the following, we shall compare and examine the resultant

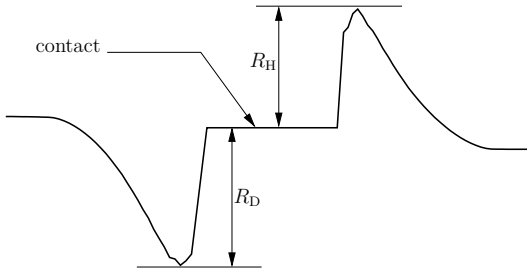

Figure 7: Schematic representation of the surface roughening and the definition of material pile-up height R_{H} and material sink-in depth R_{D} as employed in the current work.

surface roughening profiles as obtained by finite and small strain DDP methods as well as crystal plasticity. Notice that in the current study, the rigid solid which shears the crystal is in the form of a rectangle. For studies on surface roughening including non-rectangular sliders, we refer the reader to Sundaram et al. (2012), Beckmann et al. (2014) and Brinckmann and Dehm (2015).

The finite and small strain DDP results of surface profiles for widths of $W = 1.0$ μm and $W = 4.0$ μm are shown in Figs. 8(a) and (b) at $u_1 = 0.04$ μm. The corresponding crystal plasticity results are also included here. A comparison between the CP results in these figures shows that the height of the material pile-up and the depth of the material sink-in and their widths are all larger for the $W = 1.0$ μm case. This is due to the fact that for the contact size of $W = 4.0$ μm plastic deformation is mostly concentrated under the rigid solid where the material is more constrained. On the contrary, for the case of $W = 1.0$ μm a large part of plastic slip occurs towards the free surfaces surrounding the contact region. The same features are

also captured by both the DDP methods with the difference that a wider portion of the surface has been affected by roughening. This is due to the fact that in the DDP calculations the plastic zone is broader as in these simulations the availability of nucleation sources limits the amount of plasticity that can be achieved locally. However, plastic deformation in CP calculations occurs at every material point where the shear strength was exceeded and therefore, compared to DDP, plasticity is more localized. Figure 8 also demonstrates that while in CP calculations, for a single W the magnitudes of R_{D} and R_{H} are visually the same, these values distinctly differ from each other in DDP. The surface profiles due to elastic deformations are given in Appendix A.

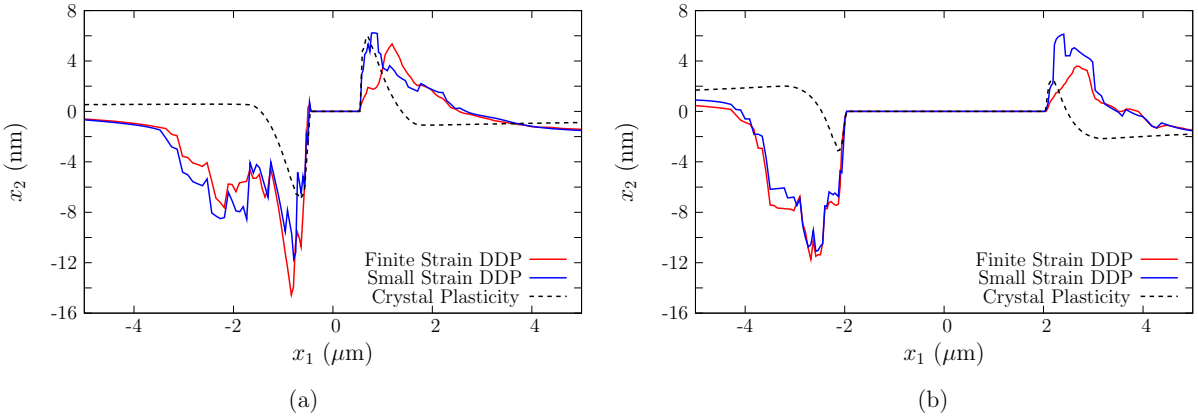

Figure 8: Finite and small strain DDP and crystal plasticity results of surface profiles for contact sizes of (a) $W = 1.0$ μm and (b) $W = 4.0$ μm at deformation of $u_1 = 0.04$ μm. The DDP calculations are carried out for the same realisation.

The results in Figs. 8(a) and (b) also illustrate that finite strain DDP calculations lead to a relatively smoother surface profile with fewer sharp points. This is because in the small strain calculations, the nucleated dislocations gliding on the same slip plane leave the crystal from the same point on the surface. In a finite strain study, however, the location of exit for dislocations of the same slip plane changes slightly with continued deformation and this leads to a smoother surface profile. The profiles obtained by crystal plasticity calculations are completely smooth, since they are not based on discrete slip systems and lack crystallographic steps.

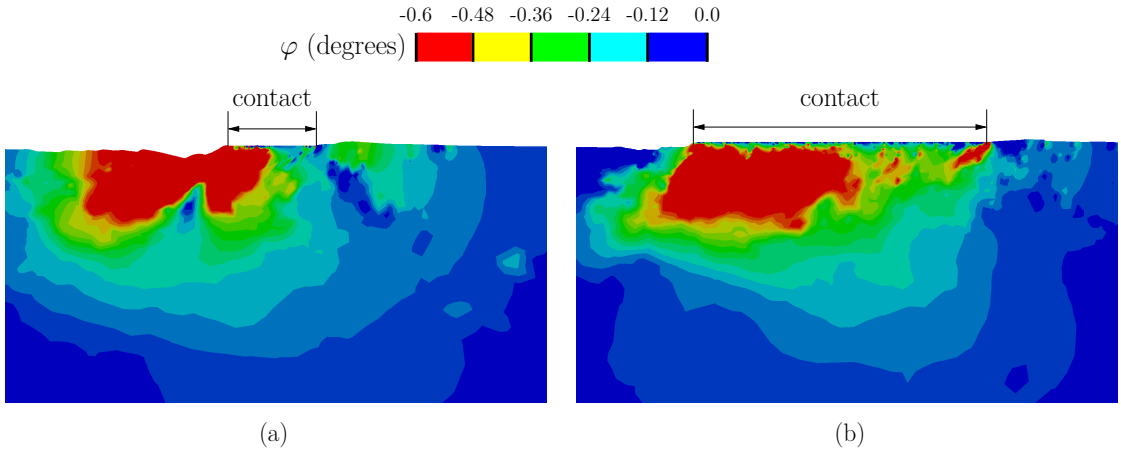

Figure 9: Finite strain DDP predictions of lattice rotation φ at an applied displacement $u_1 = 0.04$ μm for contact sizes of (a) $W = 1.0$ μm and (b) $W = 4.0$ μm. The results are plotted on the deformed configuration where the deformation is magnified by 10.

Finite strain DDP results of lattice rotation φ for widths of $W = 1.0$ μm and $W = 4.0$ μm are shown in Figs. 9(a) and (b). One may observe that the difference between large and small contact sizes also manifests itself in the resultant lattice rotation contours. As it can be seen, the area affected by lattice rotations is more confined to the contact region for the $W = 4.0$ μm case. It is worth mentioning that, different from the case of wedge indentation (Zhang et al., 2014), removing obstacles from the DDP calculations does not affect the lattice misorientation distribution.

To further elaborate on the above-mentioned trends, finite and small strain DDP calculations of the variation of normalized material pile-up height R_{H}/W and sink-in depth R_{D}/W with displacement u_1 are given in Figs. 10(a) and (b), respectively. These figures demonstrate that with the advent of plasticity, the

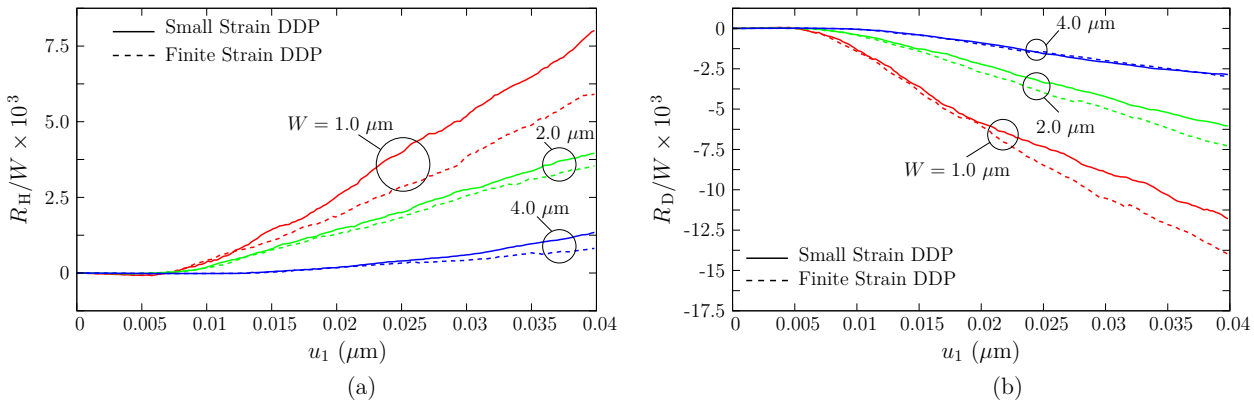

Figure 10: Finite and small strain DDP results of normalized (a) material pile-up height R_{H}/W and (b) material sink-in depth R_{D}/W vs. lateral displacement u_1. Results are shown for three selected widths W of the shearing solid.

magnitude of the roughening parameters starts to increase with applied displacement. The values of R_{H}/W and R_{D}/W are size dependent with the smallest width W resulting in largest absolute values. Furthermore, similar to the shearing response, the difference between small and finite strain calculations decreases with contact size. Therefore, allowing for finite strain effects not only results in smaller plastic hardening but also in a different surface profile for relatively small contact sizes.

4.1. Effect of crystal orientation

We now will repeat our calculations for the crystal of Section 3.1 obtained by mirroring the reference crystal with respect to the X_2−X_3 plane. The finite and small strain DDP predictions of pile-up height R_{H}/W and sink-in depth R_{D}/W are shown in Figs. 11(a) and (b). By contrasting this figure with Fig. 10, an opposite trend is observed: By mirroring the crystal orientations the ranges of R_{H}/W and R_{D}/W have swapped and the depth of the valley at the rear of contact is less than the height of the material pile-up. Furthermore, contrary to the results obtained for the reference crystal, here, the finite strain curves of maximum peak in pile-up and deepest valley in sink-in both fall above their small strain counterparts.

The surface profiles obtained by finite strain DDP and crystal plasticity are presented in Fig. 12(a) for $W = 1.0$ μm. In the previous section, it was shown that CP surface profiles have similar values for R_{D} and R_{H}. Hence, contrary to DDP, the CP simulations lead to surface profiles that are insensitive to crystal orientation. In addition, Fig. 12(b) illustrates that the resultant lattice rotation distribution is also mirrored along with the crystal orientation.

A comparison between the results obtained for the two crystals employed in this work shows that the distribution of lattice rotation and the surface profile are both sensitive to the orientation of slip even though the shear response is not. Therefore, it is possible to find orientations which give less roughening while keeping the plastic shearing strength constant.

To obtain a guideline for controlled ploughing and wear, it is of interest to find a relation between the resultant surface profile and the crystallographic orientation. In the study of indentation of mono-

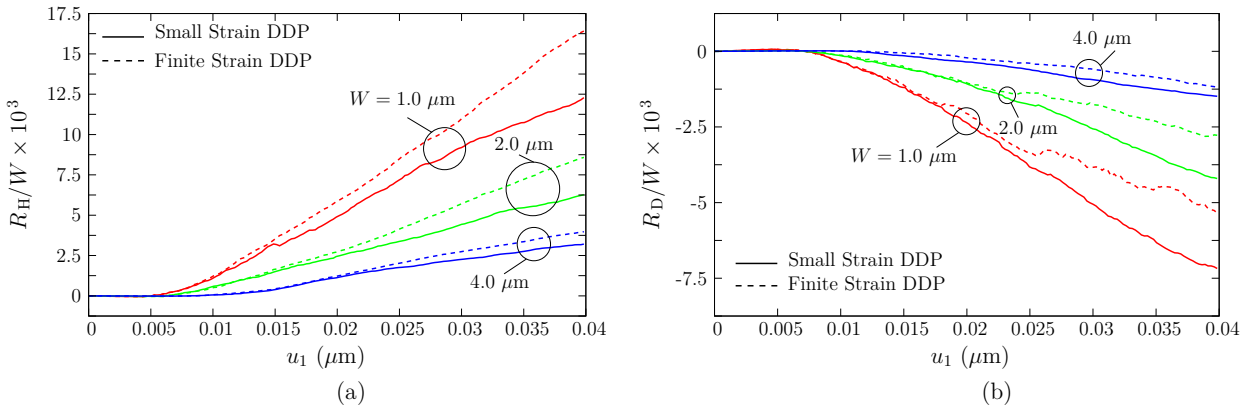

Figure 11: Finite and small strain DDP results of normalized (a) material pile-up height R_H/W and (b) material sink-in depth R_D/W vs. lateral displacement u_1. Results are shown for three selected widths W of the shearing solid.

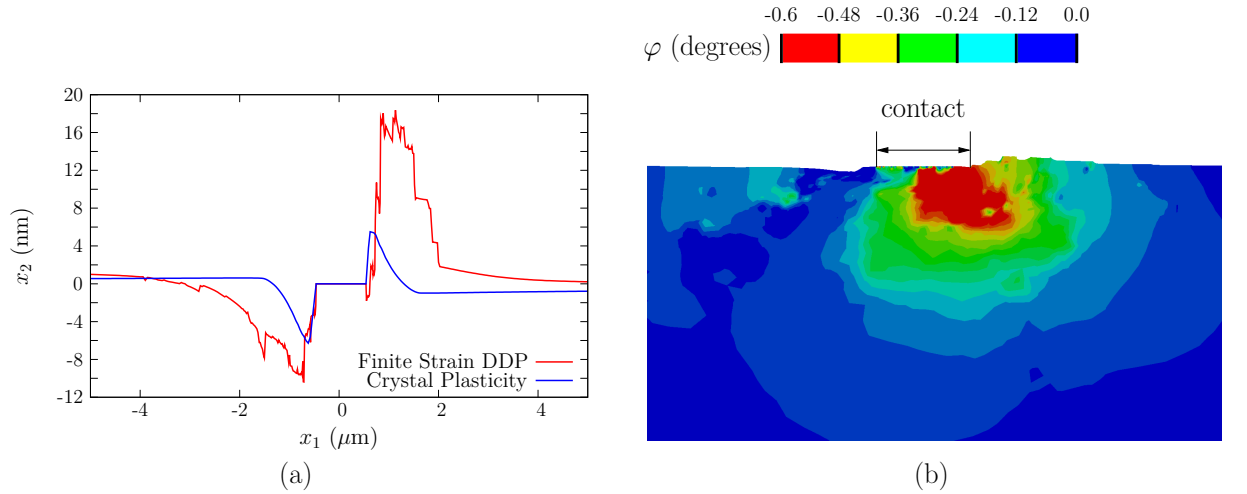

Figure 12: (a) Comparison between finite strain DDP and crystal plasticity results of surface profiles and (b) finite strain DDP predictions of lattice rotation φ at an applied displacement $u_1 = 0.04$ μm for a width of $W = 1.0$ μm and a particular realisation. The results in (b) are plotted on the deformed configuration where the deformation is magnified by 10.

crystals, Peralta et al. (2004) showed that material sink-in is present in regions where at least two slip traces intersect, whereas material pile-up is typical of single slip. Moreover, performing CP simulations of indentation, Bouvier and Needleman (2006) showed that both sink-ins and pile-ups may occur in crystals with a single soft slip system. Here, to simplify our problem, we will also start by considering the effect of a single slip system on the surface profiles obtained by shearing.

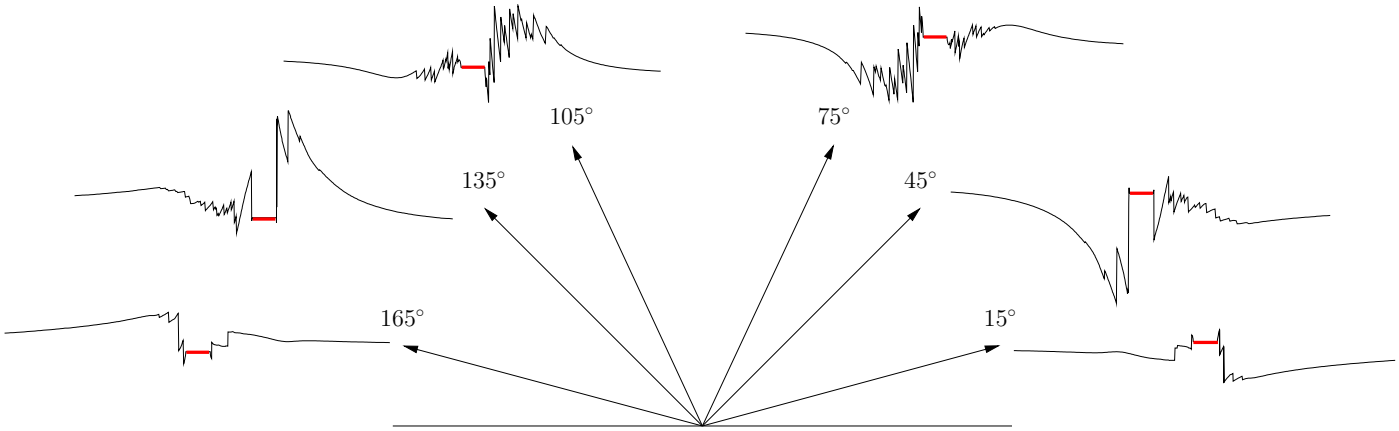

Figure 13: Finite strain DDP predictions of surface profiles for a rigid body width of $W = 1.0$ μm and crystals with single slip system. The employed slip system orientation is shown beside the corresponding figure and the contact is highlighted in red. The results are shown for an applied displacement $u_1 = 0.04$ μm with the u_2 displacements being magnified by 400.

To this end finite strain DDP simulations have been performed for different slip orientations varying from $\phi_1 = 15°$ to 165° and a rigid body width of $W = 1.0$ μm. Figure 13 illustrates that the angle between the direction of shearing and the orientation of slip plays a key role in the determination of the surface roughening profiles. The results obtained for acute angles ($\phi_1 < 90°$) show that the depth of the sink-in behind the contact increases with slip system angle as ϕ_1 rises from 15° to 45°. The sink-in becomes less deep for the slip direction $\phi_1 = 75°$. For obtuse angles ($\phi_1 > 90°$), however, the material pile-up in front of the contact is the dominant feature of the surface profiles with the height of the material pile-up being maximum when $\phi_1 = 135°$. These calculations show that in a two dimensional analysis, a distinct material sink-in behind the contact and a material pile-up in front of it form if at least two slip systems are active: one forming an acute angle and the other an obtuse angle with the loading direction.

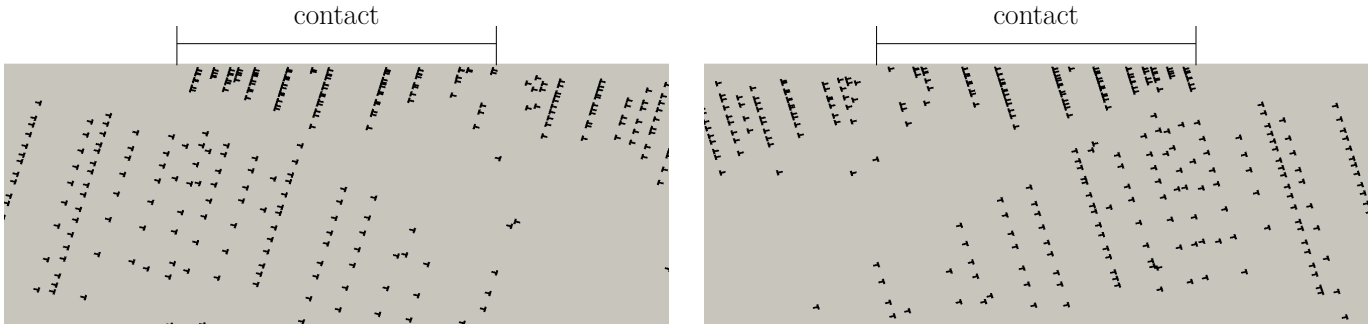

Figure 14: Finite strain DDP predictions of dislocation structure at an applied displacement $u_1 = 0.04$ μm for single-slip orientation crystals with (a) $\phi_1 = 75°$ and (b) $\phi_1 = 105°$.

The dislocation patterns of the single-slip orientation crystals with $\phi_1 = 75°$ and $\phi_1 = 105°$ are presented in Figs. 14(a) and (b), respectively. In the $\phi_1 = 75°$ crystal, pile-ups of positive dislocations form at the rear

of the contact region as the negative dislocations have left the domain, creating a sink-in behind the contact. Conversely, in the $\phi_1 = 105^\circ$ crystals, the developed strain gradients dictate the negative dislocations to leave *in front* of the contact, forming a material pile-up ahead of it.

Going back to the reference crystal with three slip systems, the slip Γ contours in Fig. 3 indicate that the material pile-up ahead of the contact is due to the dislocations exiting from $\phi_3 = 135^\circ$. In addition, a sink-in is formed at the rear of contact, mostly due to dislocation activities on $\phi_2 = 75^\circ$ slip systems. Finally, shearing a crystal with three active slip systems where two of the slip systems have acute angles results in a surface profile where the depth of the sink-in is larger than the height of the material pile-up.

4.2. Effect of nucleation source density

Becker (1998) stated that when poly-crystals are under uniaxial loading, a softer plastic response manifests itself by increased surface roughening. He showed that a plastically softer material admits strain localization more readily. As a result of this, material sink-ins develop earlier and deeper when compared to what is observed in harder materials.

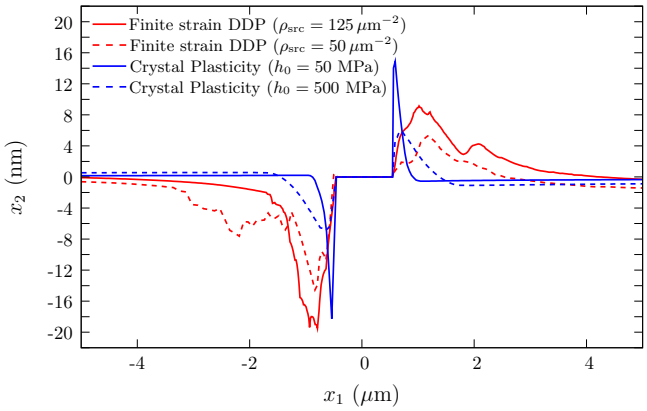

Figure 15: Finite strain DDP and crystal plasticity results of surface profiles for a contact size of $W = 1.0$ μm. The single crystal is identified by $\rho_{nuc} = 125\,\mu m^{-2}$ and $50\,\mu m^{-2}$ in the finite strain DDP simulations and $h_0 = 50$ MPa and 500 MPa in the crystal plasticity calculations.

In Section 3.2, it was shown that increasing the nucleation source density from $50\,\mu m^{-2}$ to $125\,\mu m^{-2}$ results in a softer shear plastic response. The finite strain DDP surface profile for the cases of $\rho_{nuc} = 50\,\mu m^{-2}$ and $125\,\mu m^{-2}$ are shown in Fig. 15. The CP calculations corresponding to materials with strength of slip systems $h_0 = 50$ MPa and $h_0 = 500$ MPa are also included in this figure. Here, the crystal plasticity parameters are chosen to fit the DDP calculation. This figure illustrates that for crystals with a lower plastic hardening response both material pile-up height R_H and sink-in depth R_D are larger while the region affected by roughening is smaller.

5. Conclusions

In this paper, we present the analysis of the contact shearing of an FCC single crystal by a rigid solid. The plastic shear response and the resultant surface roughening are studied by both the finite and small strain discrete dislocation plasticity (DDP) methods to examine the influence of finite deformation on plasticity and surface roughening. Crystal plasticity (CP) results are also presented as a mean of comparison and to asses the validity of this method to study plasticity of single crystals upon contact shearing. This study leads to the following conclusions:

During plastic shearing of FCC crystals, surface roughening takes place with material piling up in front of the contact and sinking in behind it. Pile-ups and sink-ins are captured by all methods used in this

work, including crystal plasticity simulations. However, only discrete dislocation plasticity predicts crystallographic steps on the surface, associated with dislocations gliding outside of the free surfaces. The size of the pile-ups and sink-ins are found to be much larger in discrete dislocation plasticity when compared to crystal plasticity, where plastic deformation is more localized because there are no limitations to the number of plastic carriers as in DDP. Also, contrary to crystal plasticity, DDP predicts a strong crystal-orientation dependence of the pile-ups and sink-ins. The shear stress in the material is instead found to be insensitive to crystal orientation. This indicates that it is possible to select a preferential crystallographic texture to limit surface roughening, by keeping similar elastic and plastic properties.

Surface roughening is only locally affected by using a finite DDP formulation, while the major features are unchanged with respect to small strain DDP. The local differences are caused by the fact that in the finite strain formulation the location of exit for dislocations of the same slip plane changes slightly with continued deformation.

The largest difference between the results obtained by small and finite DDP is in terms of plastic flow. The finite strain calculations, compared to the small strain simulations, typically correspond to a larger plastic slip and hence, a smaller shear flow strength. However, the difference between finite and small strain calculations becomes negligible for large contacts and high dislocation source densities, as both cases lead to pronounced plastic slip. When plasticity is limited, dislocations pile-up on few slip planes and dislocation glide is limited. These pile-ups are strong, straight, and associated with the strong back-stress in small strain plasticity, while they are curved and shorter in finite strains, allowing for more plastic glide.

Appendix A. Finite strain effects in elastic shearing

Finite and small strain elastic results of contact shear stress τ versus lateral displacement u_1 are presented in Fig. A.1(a) for the cases of $W = 1.0$ μm, 2.0 μm and 4.0 μm. Over the range of lateral displacements

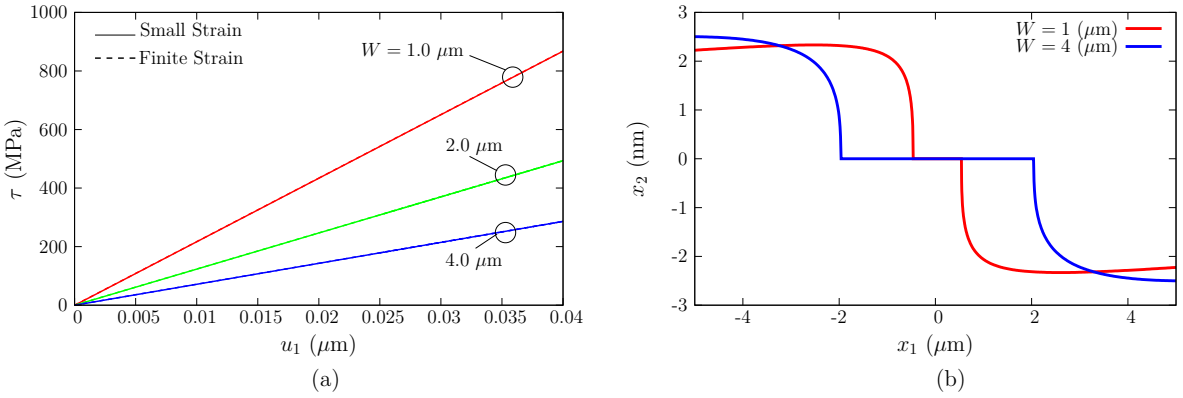

Figure A.1: (a) Finite and small strain elastic predictions of contact shear stress τ vs. lateral displacement u_1 for rigid body widths of $W = 1.0$ μm, 2.0 μm and 4.0 μm. (b) Elastic surface deformations at an applied displacement $u_1 = 0.04$ μm for rigid body widths of $W = 1.0$ μm and 4.0 μm.

investigated here there is a negligible difference between the small and finite strain elastic results. This is due to the fact that the dimensions of the specimen are relatively large (1000 μm $\times$50 μm) when compared to the applied displacements and the contact size. As a result of this the rotations and the deformations developed in the domain are very small. Therefore, the differences between the finite and small strain DDP simulations as seen in Section 3 are solely caused by finite strain discrete dislocation plasticity effects.

The elastic surface deformations at an applied displacement $u_1 = 0.04$ μm are shown in Fig. A.1(b) for rigid body widths $W = 1.0$ μm and 4.0 μm. The differences between these surface profiles and their plastic counterparts stem from the fact that in an elastic study, surface deformations are solely a result of the imposed deformations and rotations as there is no dislocation activity present.

Appendix B. Indentation results

Finite and small strain DDP results of contact normal stress σ versus normal displacement $|u_2|$ are shown in Fig. B.1(a) for the cases of $W = 1.0$ μm, 2.0 μm and 4.0 μm. Here, in order to calculate the contact

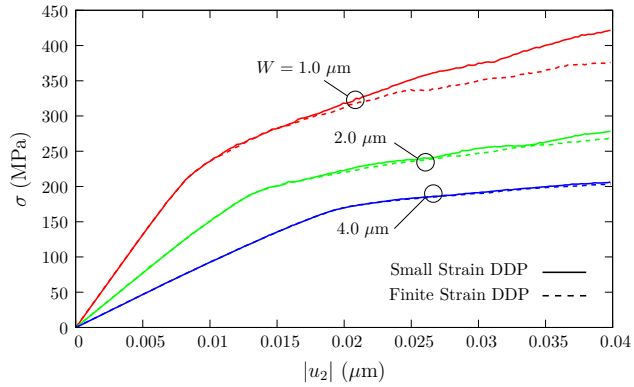

Figure B.1: Finite and small strain DDP results of nominal normal stress σ vs. normal displacement $|u_2|$. Results are shown for three selected indenter widths W.

normal stress we have employed the following relation:

$$\sigma = \frac{1}{W}\left|\int_{S_C} T_2 \, \mathrm{d}s\right|, \tag{B.1}$$

where the integration is performed along the contact area $S_C = \{-W/2 \leq X_1 \leq W/2 \text{ and } X_2 = 0\}$ and T_2 are the tractions in the X_2 direction. This figure shows that in the plastic regime, compared to their finite strain counterparts, the small strain DDP simulations present a harder response. Furthermore, analogous

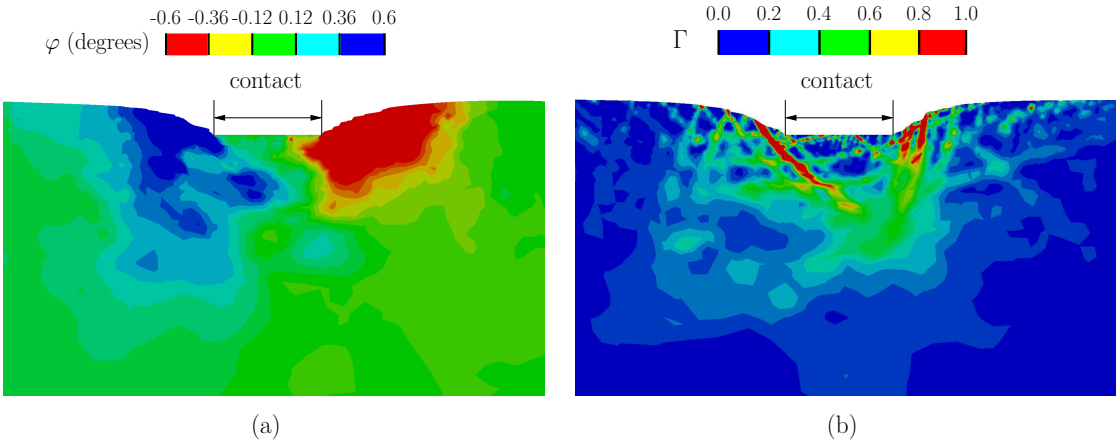

Figure B.2: Finite strain DDP predictions of (a) lattice rotation φ and (b) the employed measure of total slip Γ at an applied displacement $|u_2| = 0.04$ μm for indenter width of $W = 1.0$ μm and a particular realisation. Both results are plotted on the deformed configuration where the deformation is magnified by 10.

to the case of shearing, the difference between the small and finite strain predictions decreases with indenter width. However, by comparing Figs B.1(a) and 2(a) one may observe that the difference between the results obtained by finite and small strain DDP calculations are smaller in the case of indentation. The finite strain DDP predictions of lattice rotation φ for the contact size of $W = 1.0$ μm are shown in Fig. B.2(a). The corresponding results of total slip Γ are demonstrated in Fig. B.2(b). It is shown that in the case of indention

lattice rotations develop in both clockwise and counter clockwise directions, in contradiction with the case of shearing where the dislocations pile-ups accommodate solely to a clockwise lattice rotation. Besides, the Γ contours show that here, the formed slip bands are relatively shorter when compared to their shear counter parts. Hence, in the case of indentation the observed difference between the small and finite strain DDP predictions is less.

Conflict of interest statement

The authors have no conflicts of interest to disclose.

Acknowledgements

LN received funding from the European Research Council (ERC) under the European Union's Horizon 2020 research and innovation programme (grant agreement no. 681813). LN also acknowledges support by the Netherlands Organisation for Scientific Research NWO and Dutch Technology Foundation STW (VIDI grant 12669).

References

Balint, D. S., Deshpande, V., Needleman, A., Van der Giessen, E., 2006. Size effects in uniaxial deformation of single and polycrystals: a discrete dislocation plasticity analysis. Modelling and Simulation in Materials Science and Engineering 14 (3), 409.

Becker, R., 1998. Effects of strain localization on surface roughening during sheet forming. Acta Materialia 46 (4), 1385–1401.

Beckmann, N., Romero, P., Linsler, D., Dienwiebel, M., Stolz, U., Moseler, M., Gumbsch, P., 2014. Origins of folding instabilities on polycrystalline metal surfaces. Physical Review Applied 2 (6), 064004.

Bouvier, S., Needleman, A., 2006. Effect of the number and orientation of active slip systems on plane strain single crystal indentation. Modelling and Simulation in Materials Science and Engineering 14 (7), 1105.

Brinckmann, S., Dehm, G., 2015. Nanotribology in austenite: Plastic plowing and crack formation. Wear 338, 436–440.

Deshpande, V., Needleman, A., Van der Giessen, E., 2004. Discrete dislocation plasticity analysis of static friction. Acta materialia 52 (10), 3135–3149.

Gagel, J., Weygand, D., Gumbsch, P., 2018. Discrete dislocation dynamics simulations of dislocation transport during sliding. Acta Materialia 156, 215–227.

Irani, N., Remmers, J. J., Deshpande, V. S., 2017. Finite versus small strain discrete dislocation analysis of cantilever bending of single crystals. Acta Mechanica Sinica, 1–15.

Irani, N., Remmers, J. J. C., Deshpande, V. S., 2015. Finite strain discrete dislocation plasticity in a total lagrangian setting. Journal of the Mechanics and Physics of Solids 83, 160–178.

Karthikeyan, S., Kim, H., Rigney, D., 2005. Velocity and strain-rate profiles in materials subjected to unlubricated sliding. Physical review letters 95 (10), 106001.

Kubin, L. P., Canova, G., Condat, M., Devincre, B., Pontikis, V., Brechet, Y., 1992. Dislocation microstructures and plastic flow: a 3d simulation. Solid State Phenomena 23-24, 455–472.

Ng Wei Siang, K., Nicola, L., 2017. Static friction of sinusoidal surfaces: a discrete dislocation plasticity analysis. Philosophical Magazine, 1–18.

Peirce, D., Asaro, R. J., Needleman, A., 1983. Material rate dependence and localized deformation in crystalline solids. Acta metallurgica 31 (12), 1951–1976.

Peralta, P., Ledoux, R., Hakik, M., Dickerson, R., Dickerson, P., Aug 2004. Characterization of surface deformation around vickers indents in monocrystalline materials. Metallurgical and Materials Transactions A 35 (8), 2247–2255.

Rigney, D. A., Karthikeyan, S., 2010. The evolution of tribomaterial during sliding: a brief introduction. Tribology Letters 39 (1), 3–7.

Romanova, V. A., Balokhonov, R. R., Schmauder, S., 2013. Numerical study of mesoscale surface roughening in aluminum polycrystals under tension. Materials Science and Engineering: A 564, 255–263.

Song, H., Deshpande, V., Van der Giessen, E., 2016. Discrete dislocation plasticity analysis of loading rate-dependent static friction. Proceedings of Royal Society 472 (2192), 20150877.

Sun, F., van der Giessen, E., Nicola, L., 2016. Dry frictional contact of metal asperities: A dislocation dynamics analysis. Acta Materialia 109, 162–169.

Sundaram, N. K., Guo, Y., Chandrasekar, S., 2012. Mesoscale folding, instability, and disruption of laminar flow in metal surfaces. Physical review letters 109 (10), 106001.

Van der Giessen, E., Needleman, A., 1995. Discrete dislocation plasticity: a simple planar model. Modelling and Simulation in Materials Science and Engineering 3, 689–735.

Wilson, D., Roberts, W., Rodrigues, P., 1981. Effect of grain anisotropy on limit strains in biaxial stretching: Part i. influence of sheet thickness and grain size in weakly textured sheets. Metallurgical Transactions A 12 (9), 1595–1602.

Zhang, Y., Gao, Y., Nicola, L., 2014. Lattice rotation caused by wedge indentation of a single crystal: Dislocation dynamics compared to crystal plasticity simulations. Journal of the Mechanics and Physics of Solids 68, 267–279.